J-NEP: 60-band photometry and photometric redshifts for the *James Webb Space Telescope* North Ecliptic Pole Time-Domain Field

A. Hernán-Caballero[1][*], C. N. A. Willmer[2], J. Varela[3], C. López-Sanjuan[1], A. Marín-Franch[1], H. Vázquez Ramió[1],
T. Civera[3], A. Ederoclite[1], D. Muniesa[3], J. Cenarro[1], S. Bonoli[3,4,5], R. Dupke[6,7,8], J. Lim[9], J. Chaves-Montero[4],
J. Laur[10], C. Hernández-Monteagudo[11,12], J. A. Fernández-Ontiveros[1], A. Fernández-Soto[13,14], L. A. Díaz-García[15],
R. M. González Delgado[15], C. Queiroz[16,17], J. M. Vílchez[15], R. Abramo[16], J. Alcaniz[6], N. Benítez[15], S. Carneiro[18],
D. Cristóbal-Hornillos[3], C. Mendes de Oliveira[19], M. Moles[3,15], L. Sodré Jr.[19], and K. Taylor[20]

(Affiliations can be found after the references)

ABSTRACT

The Javalambre-Physics of the Accelerating Universe Astrophysical Survey (J-PAS) will observe ~1/3 of the northern sky with a set of 56 narrow-band filters using the dedicated 2.55 m Javalambre Survey Telescope (JST) at the Javalambre Astrophysical Observatory. Prior to the installation of the main camera, in order to demonstrate the scientific potential of J-PAS, two small surveys were performed with the single-CCD Pathfinder camera: miniJPAS (~1 deg² along the Extended Groth Strip), and J-NEP (~0.3 deg² around the JWST North Ecliptic Pole Time Domain Field), including all 56 J-PAS filters as well as u, g, r, and i. J-NEP is ~0.5–1.0 magnitudes deeper than miniJPAS, providing photometry for 24,618 r-band detected sources and photometric redshifts (photo-z) for the 6,662 sources with r<23.

In this paper we describe the photometry and photo-z of J-NEP and demonstrate a new method for the removal of systematic offsets in the photometry based on the median colours of galaxies, dubbed "galaxy locus recalibration". This method does not require spectroscopic observations except in a few reference pointings and, unlike previous methods, is directly applicable to the whole J-PAS survey.

We use a spectroscopic sample of 787 galaxies to test the photo-z performance for J-NEP and in comparison to miniJPAS. We find that the deeper J-NEP observations result in a factor ~1.5–2 decrease in σ_{NMAD} (a robust estimate of the standard deviation of the photo-z error) and η (the outlier rate) relative to miniJPAS for r>21.5 sources, but no improvement in brighter ones probably due to systematics. We find the same relation between σ_{NMAD} and *odds* in J-NEP and miniJPAS, which suggests that we will be able to predict the σ_{NMAD} of any set of J-PAS sources from their *odds* distribution alone, with no need for additional spectroscopy to calibrate the relation. We explore the causes for photo-z outliers and find that colour-space degeneracy at low S/N, photometry artefacts, source blending, and exotic spectra are the most important factors.

Key words. surveys - techniques:photometric - methods: data analysis - catalogues - galaxies: distances and redshifts - galaxies: photometry

1. Introduction

The Javalambre-Physics of the Accelerating Universe Astro-physical Survey (J-PAS; Benítez et al. 2009, 2014) will observe thousands of square degrees in the Northern hemisphere with a unique set of 56 optical filters that provides, for each 0″48×0″48 pixel on the sky, an R~60 photo-spectrum (hereafter j-spectrum) covering the 3800–9100 Å range. This will enable achieving the extremely accurate photometric redshifts (photo-z), needed to measure the cosmological baryonic acoustic oscillation (BAO) signal across a wide range of cosmic epochs, and to characterise millions of stars, galaxies and quasars to a level of detail previously restricted to spectroscopic studies.

The instrument that makes J-PAS possible, JPCam, has 14 CCDs (each containing 9200×9200 pixels) covering an area of ~4.2 deg² in a single pointing. JPCam is currently being commissioned on the 2.5 m JST/T250 telescope at the Observatorio Astrofísico de Javalambre (OAJ; Cenarro et al. 2014).

Prior to the installation of JPCam, a single-CCD camera (Pathfinder) was used on the JST/T250 telescope to start its scientific operation and to provide observations with the same filter set of J-PAS in advance of the actual survey. Most of the observing time with Pathfinder was devoted to performing a ~1 deg² survey of the Extended Groth Strip with

---

[*] email: ahernan@cefca.es

the 56 filters of J-PAS along with u, g, r and i, reaching depths comparable to those expected for J-PAS (Bonoli et al. 2021). This survey, dubbed miniJPAS, has been used to test the performance of the telescope and the Pathfinder camera (Bonoli et al. 2021; Xiao et al. 2021), the algorithms for detection of emission lines (Martínez-Solaeche et al. 2021; Iglesias-Páramo et al. 2022), star/galaxy/quasar classification (Baqui et al. 2021; Queiroz et al. 2022), and photo-z calculation (Hernán-Caballero et al. 2021; Laur et al. 2022), as well as to obtain the first scientific results on the properties of J-PAS galaxies (González Delgado et al. 2021, 2022; Martínez-Solaeche et al. 2022; Rodríguez-Martín et al. 2022) and quasars (Chaves-Montero et al. 2022).

A second survey performed with Pathfinder is the Javalambre North Ecliptic Pole Survey (J-NEP). Like miniJPAS, J-NEP uses the 56 filters of J-PAS plus u, g, r, and i. It consists of a single Pathfinder pointing (~0.3 deg²) but with significantly longer total exposure times, reaching between ~0.5 and ~1.0 magnitudes deeper than miniJPAS (see Sect. 2).

J-NEP covers entirely the *James Webb Space Telescope* (JWST) North Ecliptic Pole Time-Domain Field (JWST-TDF; Jansen & Windhorst 2018). The JWST-TDF is a new extragalactic field of interest selected for its low Galactic extinction, absence of bright stars, and location within the Northern continuous viewing zone of JWST. The guaranteed time program

JWST-GTO-2738 (PI: Windhorst) has been awarded ~47 hours to imaging the JWST-TDF in 8 filters with JWST/NIRCam and JWST/NIRISS slit-less spectroscopy in parallel, drawing a 4-spoke pattern (Fig. 1). The multi-wavelength coverage ranges from hard X-rays to radio wavelengths as tabulated by R. Jansen[1]. It includes: broad-band imaging in the optical and near-infrared with the *Hubble Space Telescope* (PI: Jansen), *Subaru* (PIs: Hasinger & Hu), and the *Gran Telescopio Canarias* (PI: Dhillon); X-rays with *NuSTAR* (PI: Civano) and *Chandra* (PI: Maksym); submillimetre observations with the *James Clerk Maxwell Telescope* (PIs: Smail & Im) and *IRAM 30m* (PI: Cohen), radio observations with the *Very Large Array* (PIs: Windhorst & Cotton), *Very Long Baseline Array* (PI: Brisken), and the *Low-Frequency Array* (PI: Van Weeren), among others.

A significant effort to obtain spectroscopy in the JWST-TDF is also ongoing. Willmer et al. (in prep.) obtained 1553 *MMT*/Binospec spectra covering the ~3900–9350 Å wavelength range, 1013 of them yielding high confidence spectroscopic redshifts. However, for the majority of sources within the J-NEP footprint, photo-z will be the only redshift estimates available in the foreseeable future. The J-NEP j-spectra will thus play an important role in the characterisation of many of the sources detected in the multi-wavelength surveys.

Unlike miniJPAS and J-NEP, most of the area that will be covered by J-PAS lacks any substantial spectroscopic coverage at the depth required to validate the photo-z ($r\sim23$). As a consequence, the strategies for prediction of the photo-z performance and for removal of systematic offsets in the photometry (see Hernán-Caballero et al. 2021, hereafter HC21) need to be made independent from the availability of spectroscopy at a given pointing.

In this paper, we present the photometry and photo-z of the J-NEP survey. In preparation for J-PAS, and in contrast to miniJPAS, the photo-z of J-NEP have been obtained independently of any spectroscopic information in all the steps of the process (the team responsible for the data reduction, photometry, and photo-z calculation only had access to the spectroscopic data after delivery of the final photo-z catalogue). This eliminates the possibility of overestimating the actual photo-z accuracy that in miniJPAS could result from the overlap among the spectroscopic samples used for template selection, photometric recalibration, and photo-z validation.

Section 2 describes the J-NEP observations, the data reduction and calibration, as well as the spectroscopic redshifts used to validate the J-NEP photo-z. Section 3 discusses the star/galaxy classification of J-NEP. In Sect. 4, we present the methodology for photo-z calculation and compare the distribution of photo-z in J-NEP and miniJPAS. In Sect. 5, we evaluate the accuracy of photo-z in J-NEP using the spectroscopic subsample, compare them to miniJPAS, and extrapolate to the entire J-NEP sample. Sect. 6 discusses the causes for photo-z outliers and Sect. 7 summarises our conclusions. All magnitudes are presented in the AB system.

2. Observations and data reduction

2.1. J-NEP observations

The J-NEP survey is centred at (RA, Dec) = ($17^h22^m26^s$,+$65^d46^m48^s$), covering the entirety of the JWST-TDF footprint as well as most of the ancillary observations (see Figure 1). Observations of the J-NEP were carried out
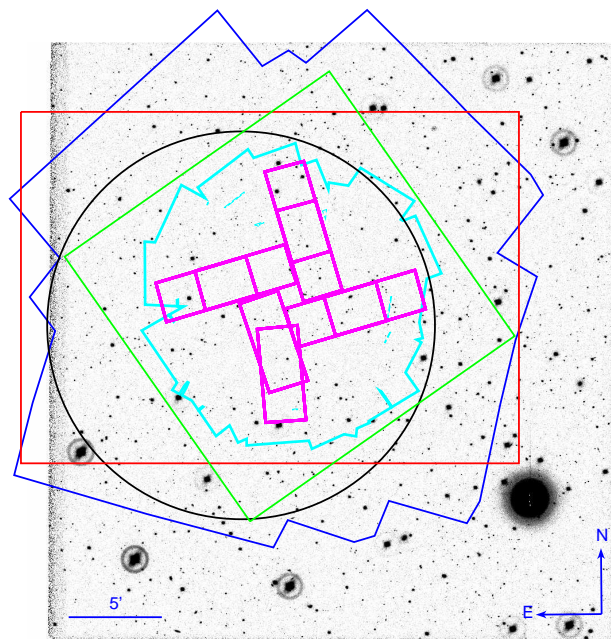

Fig. 1. Co-added *r*-band image from J-NEP. The 4-spoke pattern in magenta indicates the regions with NIRCam+NIRISS coverage from the JWST-GTO-2738 program (see Jansen & Windhorst 2018, for details), including fields observed in 2022 (southern and eastern spokes) and planned for 2023 (northern and western). Other lines mark the footprint of ancillary observations with HST/ACS+WFC3 (cyan polygon), NuSTAR (dark blue polygon), Chandra (green square), VLA (black circle), and the area covered by spectroscopic observations with MMT/Binospec (red rectangle).

between 23 June 2018 and 23 July 2019. Observations in broad bands were executed every time a new set of narrow band filters were swapped, resulting in dozens of exposures in the *g*, *r*, and *i* bands. The coadded images for the *g* and *i* bands include all the exposures taken, totalling 151 images (4530 s total exposure time) and 96 images (2880 s), respectively. For the coadded image in the *r* band (which is the reference for source extraction and forced photometry, see Sect. 2.2) only the 99 images with point spread functions (PSF) full width at half-maximum (FWHM) < 1.0″ were combined, resulting in a coadded image of 2970 s exposure time. For the narrow/medium bands, the number of exposures combined ranges between 4 and 52 (total exposure times between 480 s and 6240 s). In contrast to miniJPAS, the J-NEP observations did not try to reproduce the nominal depth of J-PAS observations and the field was observed whenever possible.

Figure 2 shows the PSF FWHM of the co-added J-NEP images in each of the filters, the 5-σ depths computed from the noise in 3″ circular apertures ($mag^{5\sigma}_{AB}$), and the 50% completeness limit for point sources that is estimated by injecting simulated sources in the images ($mag^{50\%}_{AB}$). Values for the four individual miniJPAS pointings (labels AEGIS-1 to AEGIS-4) are also shown for comparison. The PSF FWHM of J-NEP ranges from 0.72″(*r* band) to 1.98″(*u* band). The FWHM is smaller than the average for miniJPAS in most of the bands, and especially in the reddest ones, which for miniJPAS were observed at low elevation (Bonoli et al. 2021). J-NEP images are also deeper due to longer total exposure times (median $\Delta mag^{5\sigma}_{AB} = 0.37$). This results in 50% completeness limits that are ~0.5 mag fainter, on average, compared to miniJPAS (median $\Delta mag^{50\%}_{AB} = 0.56$).
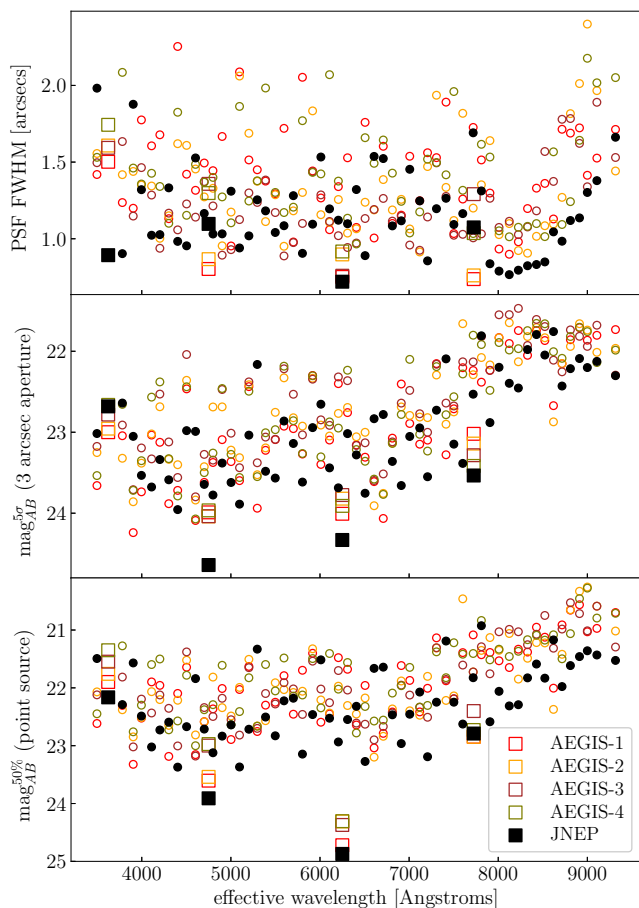
Fig. 2. Comparison of image PSF FWHM (top), depth (middle), and magnitude at 50% completeness for point sources (bottom). Solid black symbols indicate values for J-NEP, while open coloured symbols represent each of the four pointings of miniJPAS. Big squares correspond to the broad-bands u, g, r, i, while small circles correspond to the 56 bands of J-PAS.

2.2. Image processing and aperture photometry

The reduction of J-NEP images, source detection, and aperture photometry used the same procedure as for the miniJPAS. A detailed description of the full process is presented in Bonoli et al. (2021).

Data reduction for the individual images includes the standard bias and over-scan subtraction, trimming, flat fielding, and illumination correction. In the red bands, a fringing correction is also applied. Observations with the Pathfinder camera also require additional corrections for vignetting and background patterns (see Bonoli et al. 2021, for details). Astrometric calibration was performed with Scamp (Bertin 2006) using the Gaia DR2 catalogue as reference. Coaddition of the individual images was performed with Swarp (Bertin et al. 2002), with all the images resampled to the fiducial pixel scale of the camera (0.23″).

Source detection and extraction on the co-added images were performed with SExtractor (Bertin & Arnouts 1996). Aperture photometry was obtained in both dual-mode (the reference band, r, defines the aperture in which photometry is extracted for all the bands) and single-mode (source detection and extraction performed independently in each band) for several aperture types and sizes. The dual-mode catalogue contains photometry in all the filters and apertures for the 24,618 sources detected in the r-band image.

Following HC21, we use magnitudes in the AUTO aperture (2 Kron radii) as a proxy for total magnitudes. However, colour indices and photo-z are computed using PSFCOR magnitudes, which represent the magnitude that would be measured in a "restricted AUTO" aperture (1 Kron radius) if the PSF of the image were equal to the PSF of the reference band (see Coe et al. 2006; Molino et al. 2019, for a detailed description of the method).

Photometry flags from SExtractor (which indicate different issues that may degrade or invalidate the photometry) are defined separately for every source in each band. The fraction of sources affected by flags is higher than in miniJPAS (30% vs 24% for $r<23$ sources), probably due to the higher density of foreground stars (see Sect. 3).

Photometric calibration, including corrections for atmospheric extinction was performed using an adaptation of the method presented in López-Sanjuan et al. (2019a). We applied the following steps:

1) Selection of a high-quality sample of stars for calibration. We selected all J-NEP sources with a $S/N > 10$ in all photometric bands and for which a $S/N > 3$ parallax from *Gaia* DR2 is available. Using *Gaia* photometry, we constructed a diagram of the absolute G magnitude versus $(G_{BP} − G_{RP})$ colour and dereddened for dust using the 3D extinction maps from Green et al. (2018). We then selected those sources belonging to the main sequence, yielding 175 calibration stars.

2) Calibration of the images in the g, r, and i bands using the Pan-STARRS photometry as reference. We compared our 6 arcsec diameter aperture magnitudes corrected to total magnitudes with the PSF magnitudes from Pan-STARRS. The aperture corrections were computed from the light growth curves of unsaturated, bright stars in each tile and are stored in the table *jnep.TileImage* of the J-NEP database. This step provides the zero points of the images in the g, r, and i bands.

3) Calibration of the narrow bands with the stellar locus. For each narrow band, we computed the dust de-reddened $(\mathcal{X}_{ins} − r)_0$ vs. $(g − i)_0$ colour-colour diagram of the calibration stars, where $\mathcal{X}_{ins}$ is the instrumental magnitude of the selected narrow band and the extinction coefficients $k_\mathcal{X}$ were calculated for the extinction law of Schlafly et al. (2016) using the prescription in Whitten et al. (2019). We computed the offsets needed for making the J-NEP stellar locus consistent with a reference stellar locus estimated using the miniJPAS photometry. The initial offset was adjusted to account for the variation in the stellar locus position due to the different average metallicity of the calibration stars between the miniJPAS and the J-NEP pointings using the trends found by López-Sanjuan et al. (2021) in J-PLUS. This process yields the zero points of the narrow band filters. Following the results in Bonoli et al. (2021), we believe that the photometric calibration has an absolute error of at most 0.04 mag.

2.3. Recalibration with the Galaxy Locus

We compute colour indices and photo-z using the dual-mode photometry with PSF-corrected apertures (PSFCOR; see Sect. 2.2 in HC21, for details). Since PSFCOR fluxes are measured in a relatively small aperture (1 Kron radius), we scale the fluxes in all bands by a factor defined as the ratio between AUTO and PSFCOR fluxes in the r band. This makes PSFCOR magnitudes closer to total magnitudes if we dismiss the effects of radial colour gradients. The upscaling of PSFCOR fluxes is required in order to apply the correct redshift prior (which depends on the total magnitude of the source, see Sect. 4.1).

The PSFCOR photometry does not completely remove the effect of PSF variations in the co-added images in different
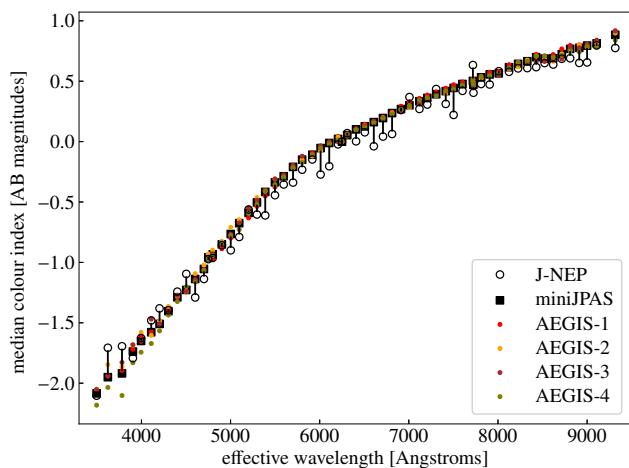
Fig. 3. Galaxy Locus for *r*<21 galaxies, defined as the median magnitude difference relative to the *r* band for each of the J-PAS bands. Coloured dots represent the Galaxy Locus obtained from the recalibrated PSFCOR photometry on individual miniJPAS pointings, while the solid squares indicate the average value in the four pointings. Open circles mark the Galaxy Locus obtained from PSFCOR photometry in J-NEP before recalibration. The segments connecting them to the squares represent the corrections required to remove systematic offsets in the PSFCOR photometry of J-NEP.

bands. This results in systematic offsets in the colours of the sources. Since accurate colours are essential for high precision photo-*z*, HC21 proposed a method for the recalibration of PSF-COR photometry using stellar population synthesis (SPS) model fits to the j-spectra of individual galaxies. In this procedure, the observed magnitudes in the J-PAS bands (corrected for atmospheric and Galactic extinction) of galaxies covering a wide redshift range are compared to synthetic photometry obtained by convolving the best-fitting SPS model for each galaxy with the transmission profiles of the filters. Systematic offsets in the photometry are computed as the median magnitude difference between the observed and synthetic photometry in each band. In an iterative process, the observed photometry is corrected by subtracting these offsets, then fitting new SPS models to the corrected photometry from which synthetic photometry is obtained and additional offsets are computed. The process converges after 3 to 4 iterations (see Sect. 3 in HC21 for details).

Such iterative SPS model fitting recalibration (hereafter, ISMFR) produces excellent results, with colours accurate to within ~0.02 mag. However, it depends critically on the availability of spectroscopic redshifts (that are needed to fit the SPS models) for a large number of galaxies in every pointing. Since the spectroscopic coverage in most J-PAS pointings will be insufficient for a recalibration à la miniJPAS, we developed an alternative recalibration strategy that we call galaxy locus recalibration (GLR). The GLR method relies on ISMFR to obtain accurate colours for the sources in some reference pointings with spectroscopy (in our case, the 4 miniJPAS pointings).

In analogy with the stellar locus, we define the galaxy locus as a set of colour indices $\{\tilde{C}_j\}$, where each element $\tilde{C}_j$ is the median colour between the *j*-th band and the *r* band

$$\tilde{C}_j = \underset{i \in R}{\mathrm{median}} \{m_i(r) - m_i(j)\} \qquad (1)$$

The set *R* indexes all the galaxies brighter than a given limit, m_{cut}. For the determination of the galaxy locus, we consider as

galaxies all the sources that have SExtractor class_star < 0.1. We set $m_{\mathrm{cut}} = 21$. There are 3067 sources in miniJPAS meeting the criteria *r*<21 and class_star < 0.1. A fainter m_{cut} increases the number of galaxies available to compute the $\tilde{C}_j$ indices, but the average uncertainty in the colours of individual galaxies also increases, particularly in the bluest bands. We find that $m_{\mathrm{cut}} \sim 21$ minimises the statistical uncertainty of the $\tilde{C}_j$.

To recalibrate J-NEP with the galaxy locus, we assume that the intrinsic colours of galaxies (that is, the colours obtained after correcting for Galactic extinction and any systematics in the photometry) are independent from the sky coordinates. Therefore, we can estimate the systematic offsets in the J-NEP photometry as $\Delta m(j) = \tilde{C}_j - \tilde{C}_j^{obs}$, where $\tilde{C}_j^{obs}$ is the "apparent" galaxy locus obtained from the observed J-NEP photometry (after correcting for Galactic extinction).

Figure 3 compares the values of the $\{\tilde{C}_j\}$ and $\{\tilde{C}_j^{obs}\}$. The difference can be as large as $|\Delta m(j)| \sim 0.3$ mag, which is consistent with the similarly large recalibration offsets obtained for miniJPAS with ISMFR (HC21). The GLR method is less accurate than ISMFR because it depends on the latter to determine the galaxy locus and is affected by other sources of uncertainty such as the statistical error in the median colours obtained from a limited sample. Cosmic variance could also introduce a systematic error in the GLR method if the galaxy population or its redshift distribution in the pointing to be recalibrated are significantly different from the reference. However, in Appendix A we evaluate each contribution to the total uncertainty of the GLR method, finding a negligible impact from cosmic variance. We predict a total systematic error in J-NEP colours of ~0.04 mag. This is a factor of ~2 worse than ISMFR achieves, but a factor of ~4–5 improvement with respect to no recalibration. To compute photo-*z*, we add this systematic error in quadrature to the photometric uncertainties.

A systematic error of ~0.04 mag in the colours implies that the photometric error dominates over systematics for most sources. The impact of the recalibration uncertainty on the photo-*z* is therefore expected to be small, except possibly for bright sources with high S/N photometry but weak spectral features, where small offsets in the photometry could mimic the effect of emission or absorption lines. In Sect. 5.1, we show what is the actual impact of this uncertainty in the photo-*z* of bright sources.

2.4. Spectroscopic observations

The spectroscopic observations were obtained using Binospec (Fabricant et al. 2019) at the MMT observatory. They used a 270 lines/mm grating which allows covering from approximately 4000 Å to 9000 Å with a typical dispersion of 1.30 Å/pixel and resolution of 1340 at the central wavelength. The sample of galaxies was selected from a combination of a preliminary catalogue coming from the HEROES Subaru HSC imaging (Hasinger, private communication) with a catalogue derived from MMT/MMIRS near-infrared imaging (Willmer et al. in preparation), limited at *r* ~ 23. The data were reduced using a specially designed pipeline that produces wavelength and flux calibrated 1-dimensional spectra (Kansky et al. 2019). Redshifts were measured using custom-written code using a combination of real-space cross-correlation and emission-line fits. All spectra were visually inspected and a redshift quality flag was assigned using the same criteria adopted by the DEEP2 survey (Newman et al. 2013), where a redshift quality of 4 (3) represents a >95% (>90%) confidence in the spectroscopic redshift.

The outputs from each of the observed fields were then merged into a single list using the positions of the near-infrared imaging, which are tied to the *Gaia* DR2 reference frame.

The spectroscopic redshift catalogue contains 1553 sources. We associate spectroscopic redshifts to J-NEP sources by looking for $r<23$ counterparts within 1″ of the spectroscopic position. We find matches for 955 sources (the remainder are either fainter than $r=23$ or outside the J-NEP footprint). The median distance of the associations is ~0.1″, with no significant systematic offset in the coordinates, and 95% of the associations are within 0.4″. For the purpose of validation of the photo-z, only robust spectroscopic redshifts (ZQUALITY≥3) are considered. This decreases the number of useful spectroscopic redshifts to 787. The spectroscopic catalogue contains no spectral classification. We consider the 58 sources with $z_{spec}<0.001$ to be likely stars and excluded them from the analysis of photo-z performance. All but six of these sources have SExtractor CLASS_STAR > 0.9 and/or point-source probabilities $P_{star} > 0.9$ (see Sect. 3). There are also 18 point sources (CLASS_STAR > 0.9 and/or $P_{star} > 0.9$) with $z_{spec}>0.001$. We inspected their spectra and found six of them to be quasars with clear broad emission lines (3 of them are detected by NuSTAR and all 6 have WISE colours consistent with a quasar). We also excluded them from the analysis. The remaining 12 point sources with $z_{spec}>0.001$ have spectra consistent with compact galaxies and remain in the validation sample.

We emphasise that the spectroscopic information was not made available to the team processing the J-NEP data until after the star/galaxy classification (see Sect. 3) and photo-z calculation (Sect. 4.1) were finished. We purposefully avoid updating the star/galaxy classification and photo-z of J-NEP sources in light of the spectroscopic information. Instead, we use the spectroscopic redshifts only for validation of the photo-z performance.

3. Star and galaxy classification

In addition to the morphological classification from SExtractor (the CLASS_STAR parameter), for every source in J-NEP we assign a probability P_{star} of being a point source using the Stellar-Galaxy Locus Classification (SGLC) described in López-Sanjuan et al. (2019b). This method uses Bayesian inference to estimate the probability of a given source being a compact object (star or quasar) from the value and uncertainty of its concentration parameter, c, defined as the difference between the 1.5″ and 3″ diameter aperture magnitudes of the source. The star probability was computed in the g, r, and i bands and the values were combined assuming independent measurements. In addition, a prior on the r-band magnitude (and for bright sources, also parallaxes from *Gaia* DR2) was applied. The resulting distribution of P_{star} is strongly bimodal, with most sources unambiguously classified as either compact or extended (see Fig. 4).

It is important to emphasise that no colour information is used in the classification. As discussed in HC21, this implies that the redshift probability distribution function $P(z)$ derived from the j-spectrum is independent of P_{star}.

Figure 5 compares the g-r and r-i colours for individual sources with $P_{star}>0.5$ and $P_{star}<0.5$. Sources more likely to be stars concentrate in a well defined arc (the stellar locus) while candidate galaxies occupy a much wider area. The distribution of the g-r and r-i colours for the spectroscopically confirmed galaxies is roughly consistent with that of the $P_{star}<0.5$ subsample.

Figure 6 compares the density of sources per unit area as a function of their r-band magnitude in J-NEP and miniJPAS. The density is computed assuming an effective footprint area (which
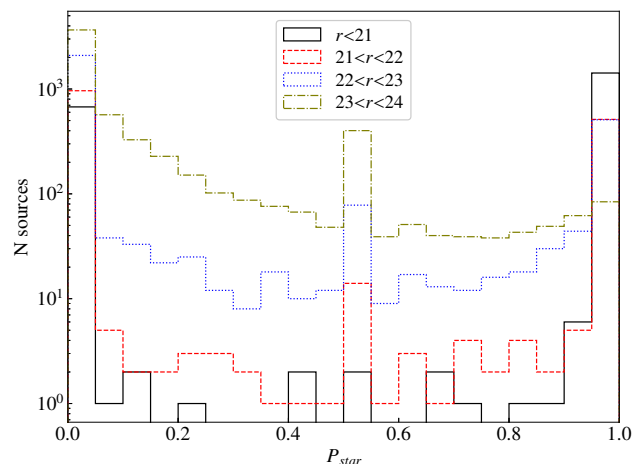

Fig. 4. Distribution of the probability of being a compact source (P_{star}) computed with the SGLC method for J-NEP sources in several magnitude intervals. The spike at $P_{star} = 0.5$ is due to sources with insufficient S/N for a classification in the detection band, which are assigned $P_{star} = 0.5$ by default.
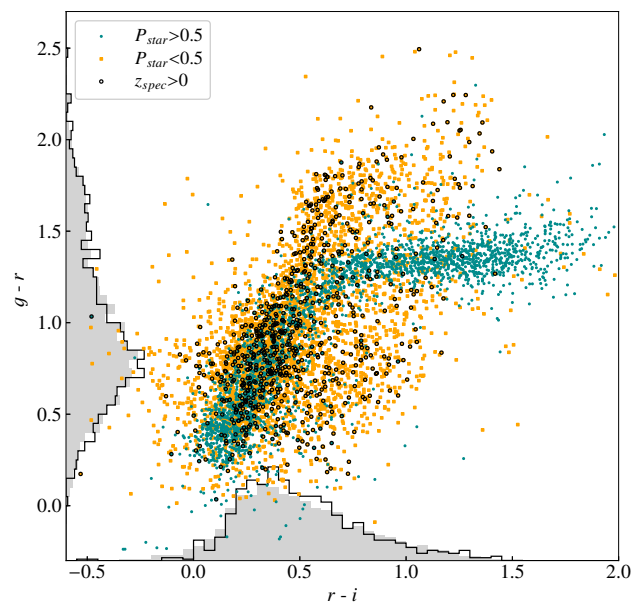
Fig. 5. Colour-colour plot including all J-NEP sources with $r<23$ and S/N>2 in the g, r and i bands. Cyan dots and orange squares represent sources morphologically classified as stars and galaxies, respectively. Black circles indicate the spectroscopically confirmed extragalactic sources (including some quasars). The solid grey and step black line histograms represent the distribution of the colours for morphologically and spectroscopically classified galaxies, respectively.

excludes masked regions) of 0.23 deg^2 for J-NEP and 0.895 deg^2 for miniJPAS. The distribution peaks at $r\sim24.5$ in J-NEP compared to $r\sim24.0$ in miniJPAS due to deeper r-band observations. The density of sources is higher in J-NEP than in miniJPAS at all magnitudes, but especially at brighter ones. We weight the individual sources with their P_{star} and $P_{gal} = 1 - P_{star}$ probabilities to produce the distributions for stars and galaxies separately. The density of stars in J-NEP is a factor of ~2 higher relative to miniJPAS due to its lower Galactic latitude. This suffices to explain the excess density of sources in J-NEP relative to miniJPAS. The
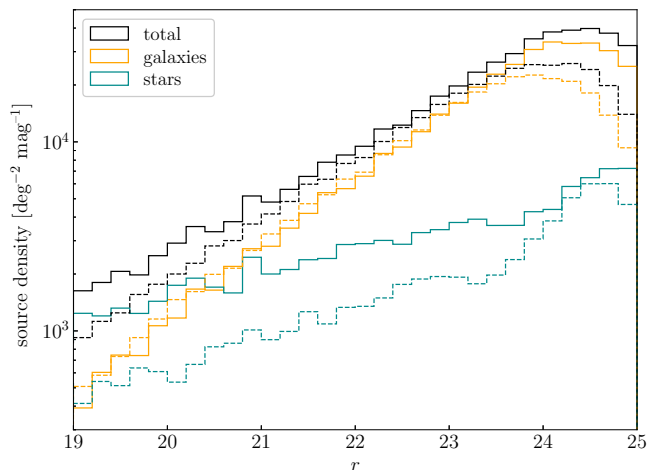
Fig. 6. Density of sources detected per unit area and magnitude as a function of their *r*-band magnitude in J-NEP (solid lines) and miniJ-PAS (dashed lines). The distributions are shown for all sources (black) as well as separately for galaxies (orange) and stars (cyan) using the probabilities P_{gal} and P_{star} as weights.

density of galaxies is consistent between the two surveys for the entire range of magnitudes up to the completeness limit of mini-JPAS ($r{\sim}23.5$). In both surveys there is an upturn in the density of stars at magnitudes fainter than their completeness limit. This is an artefact due to the assignment of $P_{star} = 0.5$ to sources that are too faint for a morphological classification.

4. Photometric redshifts

4.1. Computation of photo-z

We compute photo-*z* for all J-NEP sources with magnitude $r{\leq}23$ using the same method applied to miniJPAS, which is extensively documented in HC21. Very briefly, we use a custom version of LePhare (Arnouts, & Ilbert 2011) adapted to the properties of the J-PAS data. The galaxy templates are a set of 50 SPS models generated with CIGALE (Boquien et al. 2019). They were selected to maximise the photo-*z* performance in a subset of miniJPAS galaxies (see Sect. 4.2 in HC21). We configure LePhare to compute redshift probability distribution functions (*z*PDF) with a resolution of 0.002 in *z* and a search range $0<z<1.5$. A redshift prior derived from galaxy counts in the VIMOS VLT Deep Survey (VVDS; Le Fèvre et al. 2005) is applied to the redshift likelihood distributions to obtain the final *z*PDF.

Photo-*z* are computed for all sources regardless of their morphological classification, but only galaxy templates are used. Therefore, the *z*PDF obtained by LePhare must be considered as redshift probability distribution functions conditional to the source being a galaxy. This allows us to obtain statistics of the galaxy population not biased by the uncertainty in the star/galaxy classification (see Sects. 2.4 and 6 in HC21 for a discussion).

We emphasise that, with the exception of the recalibration strategy, all the other steps in the data processing up to and including the photo-*z* calculation use the same software packages with the exact same configuration for J-NEP and miniJPAS. Therefore, any statistical differences in the photo-*z* results must be attributed to one or more of these factors: a) differences in the quality/depth of the observations; b) systematics introduced by the recalibration; c) overestimation of the actual photo-*z* accuracy in miniJPAS due to fine-tuning of the set up in order to
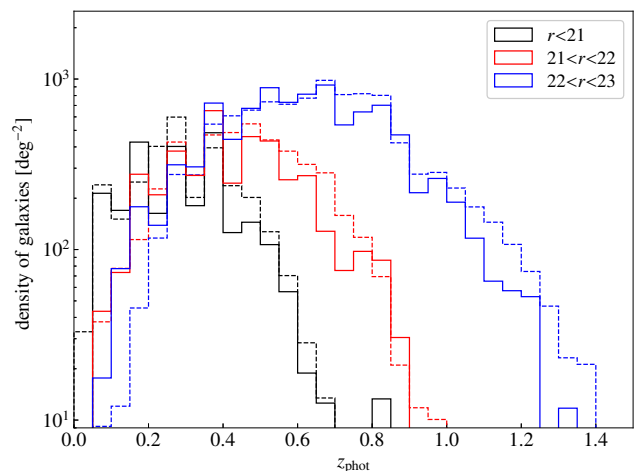
Fig. 7. Density of galaxies per unit area as a function of the most probable photometric redshift (z_{phot}) for several intervals of *r*-band magnitude in J-NEP (solid lines) and miniJPAS (dashed lines).

maximise the photo-*z* performance in the spectroscopic subsample of miniJPAS. In the next sections, we compare the photo-*z* results for J-NEP and miniJPAS to evaluate the impact of each of these factors.

4.2. Distribution of z_{phot} and *odds*

While the *z*PDF provides the most complete description of our knowledge about the redshift of a source, point estimates can be convenient for some applications. The mode of the *zPDF*, z_{phot}, which represents the redshift with highest probability density, is the most commonly used point estimate.

Another useful scalar is the *odds*, which represents the probability of the actual redshift being within a given interval around the mode. We use an interval of ±3% in 1+*z*, therefore

$$odds = \int_{z_{phot}-d}^{z_{phot}+d} P(z)dz, \qquad d = 0.03(1 + z_{phot}) \qquad (2)$$

Figure 7 compares the distribution of z_{phot} for J-NEP and miniJPAS galaxies in three magnitude intervals. As in Fig. 6, all sources are weighted with their corresponding P_{gal} to obtain the redshift distribution for galaxies.

The distributions of z_{phot} for the same magnitude interval are roughly consistent in the two surveys, but there are some interesting small differences. The brightest interval ($r<21$) shows high frequency variation with z_{phot} in the density of galaxies. For miniJPAS, HC21 showed that the peaks and valleys of the distribution of z_{phot} agree with the distribution of spectroscopic redshifts and therefore indicate real over-/under-densities at certain redshifts. In J-NEP, the small survey area implies a higher contrast of the large scale structure (LSS) signature on the redshift distribution. As expected, the over-densities traced by peaks in the distribution of z_{phot} occur at different redshifts in J-NEP and miniJPAS, but the overall shape of the distribution is very similar. The exception is the faintest interval ($22<r<23$), which shows an excess of sources at $z_{phot}<0.2$ and a deficit at $z_{phot}>1$ in J-NEP relative to miniJPAS. While we cannot rule out cosmic variance affecting the low redshift volume probed by J-NEP due to the small survey area, the deficiency of sources at high redshifts would require a strong under-density within a huge volume
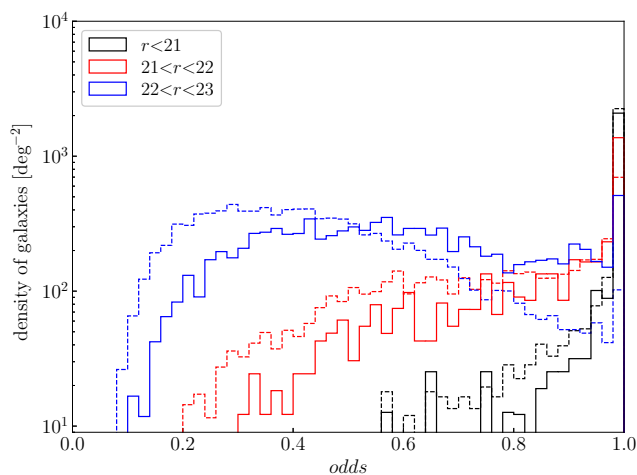
Fig. 8. Density of galaxies per unit area as a function of the *odds* parameter for several intervals of r-band magnitude in J-NEP (solid lines) and miniJPAS (dashed lines).

of the Universe. A more likely interpretation for both discrepancies is the better photo-z accuracy for $22<r<23$ sources in J-NEP relative to miniJPAS due to deeper observations. For such faint sources, the low S/N in the photometry (especially in the narrow bands) implies that the redshift prior has a strong effect in the shape of the *zPDF* and the highest probability density value. In particular, for $i=22$ ($r\sim22.5$) galaxies the probability density of the prior peaks at $z\sim0.6$–0.7 (depending on the spectral type) with a steep decrease at lower z but a flatter one at higher z (see Fig. 7 in HC21). The very low prior probability discourages $z<0.2$ solutions for faint galaxies. A higher S/N in J-NEP implies easier detection of spectral features by the template-fitting algorithm, which can help at overcoming the prior in the few faint galaxies that are actually at low z. In contrast, the flatter slope of the high-z tail of the prior is less successful at preventing wrong high-z solutions. In fact, Fig. 14 in HC21 shows that most $z_{\rm phot}>1$ galaxies in miniJPAS have $z_{\rm spec}<1$. The higher S/N in J-NEP implies that fewer $z_{\rm spec}<1$ galaxies are scattered by photometric errors into the $z_{\rm phot}>1$ region.

The higher S/N of the J-NEP photometry relative to miniJPAS at the same magnitude implies higher contrast in the *zPDF*, therefore higher *odds*, for any magnitude interval (Fig. 8). All else being equal, this should translate into a lower outlier rate for J-NEP at all magnitudes. However, the larger systematic uncertainty in J-NEP colours implies that, in sources bright enough for systematic errors to dominate over photometric errors, the outlier rate in J-NEP can be higher than in miniJPAS (see Sect. 5.1).

5. Accuracy of photo-z in J-NEP

5.1. Validation with the spectroscopic sample

In this section, we use the subsample of J-NEP with spectroscopic redshifts to evaluate the accuracy of photo-z estimates.

Figure 9 compares $z_{\rm phot}$ and $z_{\rm spec}$ values for the 554 J-NEP galaxies with reliable spectroscopic redshifts in the catalog from Willmer et al. (in preparation) and no flags in their photometry. The inset plot shows the distribution of the relative error in $z_{\rm phot}$, defined as $\Delta z = (z_{\rm phot} - z_{\rm spec})/(1+z_{\rm spec})$.

The distribution of Δz shows that $z_{\rm phot}$ systematically overestimates the actual redshift of the galaxies by a small amount
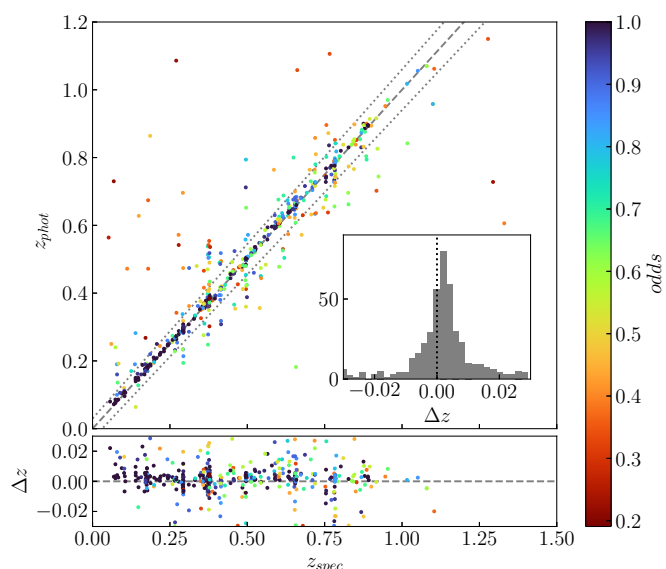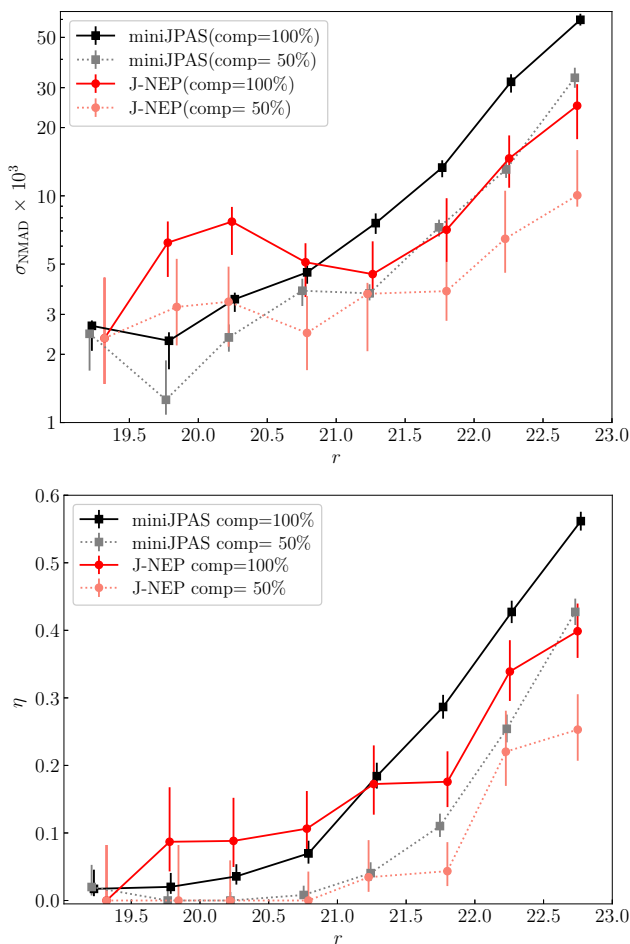

Fig. 9. Photometric redshift (top panel) and photo-z error (bottom panel) versus spectroscopic redshift for individual sources in J-NEP. Only $r<23$ sources with no photometry flags (FLAGS = 0 and MASK_FLAGS = 0) and reliable $z_{\rm spec}$ are shown. The colour coding indicates the *odds* parameter that represents the confidence in the $z_{\rm phot}$ solution. The dashed line indicates the $z_{\rm phot}=z_{\rm spec}$ relation. Dotted lines in the top panel enclose the region corresponding to $|\Delta z|<0.03$, which is enlarged in the bottom panel. The inset plot shows the distribution of Δz.
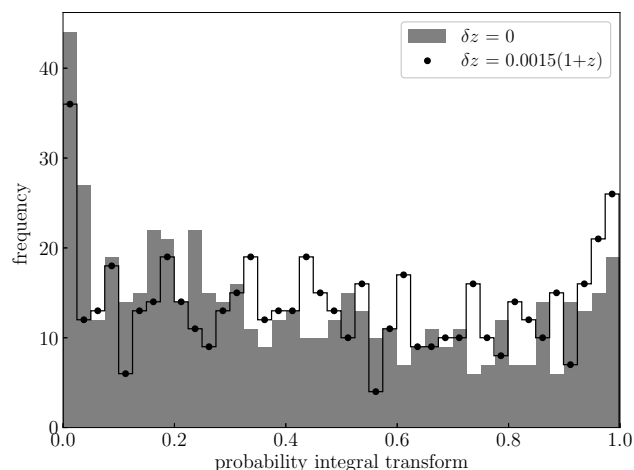
Fig. 10. Distribution of PIT values for the *zPDFs* of J-NEP galaxies with spectroscopic redshift. The solid and open histograms represent the distributions before and after correcting for a systematic offset $\delta z = 0.0015(1+z)$ in the *zPDFs*.

(median(Δz) ~ 0.1–0.2%, depending on the magnitude and *odds* cut applied and the algorithm used to reject outliers). This is consistent with the median(Δz) ~ 0.10–0.14% found in miniJPAS (HC21). The probability integral transform (PIT) diagram (Fig. 10) shows that, excluding PIT values close to 0 and 1 (which are dominated by catastrophic redshift errors, see e.g. Polsterer et al. 2016), the distribution is slightly tilted, suggesting that this bias affects the entire *zPDF*, not just its mode (this was also the case in miniJPAS). In the following analysis we correct all $z_{\rm phot}$ measurements in J-NEP and miniJPAS by subtracting $\delta z = 0.0015(1+z)$.

Fig. 12. Frequency of extreme outliers ($|\Delta z| > 0.15$) in bins of r-band magnitude for the spectroscopic subsamples of miniJPAS and J-NEP. Symbols as in Fig. 11.

Fig. 11. Normalised median absolute deviation of the photo-z error (σ_{NMAD}; top panel) and outlier rate (η; bottom panel) in bins of r-band magnitude for the spectroscopic subsamples of miniJPAS (black squares) and J-NEP (red circles). Symbols linked by solid lines represent measurements including all sources within a 0.5 mag interval in r-band magnitude, while the ones linked by dotted lines indicate the values obtained considering only the 50% of sources with higher *odds* in each magnitude bin. Error bars indicating the 16–84th percentile confidence intervals were obtained with bootstrap resampling in the case of σ_{NMAD} and the Wilson formula for binomial distributions in the case of η.

The distribution of Δz is far from Gaussian. HC21 showed that its shape is well reproduced by the combination of two Lorentzian profiles (or a Gaussian plus a Lorentzian) of very different widths. The narrow component corresponds to sources affected by small inaccuracies in the determination of the peak of the *zPDF*, while the broad component is dominated by "catastrophic errors" due to a flattened or multi-modal *zPDF*.

The typical error in z_{phot} (excluding catastrophic errors) is often represented by the σ_{NMAD} statistic, defined as

$$\sigma_{\mathrm{NMAD}} = 1.48 \times \mathrm{median}\left|\Delta z_i - \mathrm{median}(\Delta z_i)\right| \tag{3}$$

Another frequently used statistic is the outlier rate

$$\eta = \frac{N(|\Delta z| > X)}{N_{tot}} \tag{4}$$

where N_{tot} is the number of sources in the sample and $N(|\Delta z| > X)$ is the number of them having relative errors in z_{phot} larger

than a threshold X. If we choose $X = 0.03$, then the expectation value of η for the sample is related to the average *odds* by the equation

$$E[\eta] = 1 - \langle odds \rangle \tag{5}$$

While the majority of the sources in Fig. 9 are tightly packed near the 1:1 relation, 132 sources (24% of the sample) are outside the region enclosed by the dotted lines that represent an error $|\Delta z| = 0.03$. This 24% of outliers is consistent with the ~23% predicted from the mean value of their *odds* parameter, $\langle odds \rangle = 0.771$.

Figure 11 compares σ_{NMAD} and η in bins of magnitude for J-NEP and miniJPAS. Values are shown at 100% completeness (no cut in *odds* applied) and 50% completeness (only 50% of sources with higher *odds* in each magnitude bin are used to compute σ_{NMAD} and η). We note that η values for miniJPAS and J-NEP are high in part because of our restrictive criterion for outliers. Using the criterion $|\Delta z| > 0.15$ that is typical for broadband surveys results in much lower outlier rates (Fig. 12). In particular, none of the J-NEP galaxies with $r<22$ and no flags has $|\Delta z| > 0.15$.

The error bars for σ_{NMAD} and η in J-NEP are large due to the relatively small spectroscopic sample. In spite of this, we find some interesting trends. For sources fainter than $r=21.5$ both σ_{NMAD} and η are ~30–50% lower in J-NEP compared to miniJPAS at the same magnitude and completeness. This is probably a consequence of the deeper images of J-NEP and their narrower PSF, which allows for higher S/N in the photometry, in particular in the red bands (see Fig. 2).

At magnitudes brighter than $r=21$ the values of σ_{NMAD} and η are higher in J-NEP compared to miniJPAS. This suggests that for bright sources the photo-z accuracy is less sensitive to the S/N of the photometry as other factors become dominant. In particular, larger systematic errors in the recalibration with the galaxy locus relative to ISMFR implies that the total flux errors (systematic plus photometric) can be higher for bright J-NEP sources compared to miniJPAS sources of the same magnitude. However, systematics in the recalibration cannot explain a higher σ_{NMAD} at $r\sim20$ than at $r\sim21$ for J-NEP. This puzzling result might be just a consequence of small number statistics (σ_{NMAD} values for
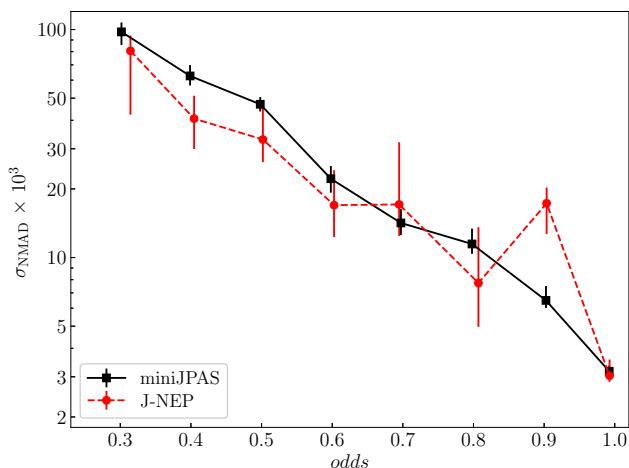
Fig. 13. σ_{NMAD} computed in bins of *odds* of width 0.1 for the spectroscopic sources in miniJPAS (squares) and J-NEP (circles). Error bars represent 1-σ confidence intervals obtained with bootstrap resampling.
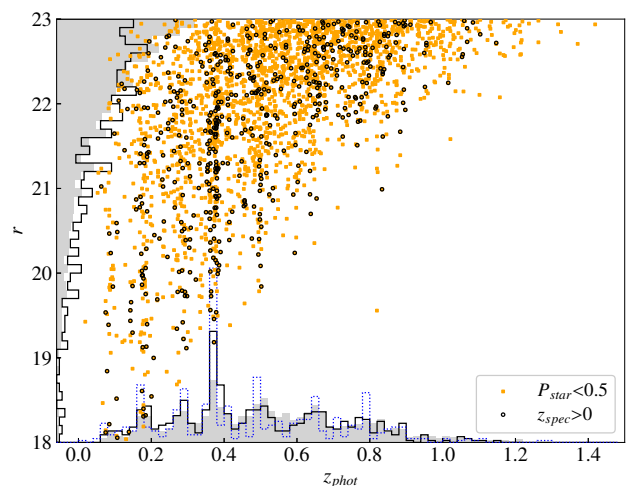

Fig. 14. Magnitude in the *r* band and the highest probability photometric redshift for individual galaxies ($P_{star}<0.5$) in J-NEP. Black circles indicate sources with spectroscopic redshift. The solid grey and step black line histograms represent the *r*-band magnitude and z_{phot} distributions for all galaxies and galaxies with spectroscopic redshift, respectively. The blue dotted histogram represents the distribution of spectroscopic redshifts in the spectroscopic subsample.

the intervals between *r*=19.5 and *r*=21.5 agree within their uncertainties). We find no clear difference in the properties of *r*~20 and *r*~21 galaxies that could explain this trend and propose further investigation when a larger spectroscopic sample becomes available. Irrespective of what is the actual photo-*z* accuracy at the bright end, the steep increase in the density of sources at fainter magnitudes implies that J-NEP has better overall accuracy than miniJPAS.

HC21 showed that the *odds* parameter is a reliable predictor of the probability of a redshift outlier and its correlation with |Δ*z*| is stronger compared to other properties such as the *r*-band magnitude. They also showed that the σ_{NMAD} within a small interval of *odds* does not have any clear residual dependence with the *r*-band magnitude, z_{spec}, or the spectral type. In Fig. 13, we compare the dependence of σ_{NMAD} with *odds* in the spectroscopic samples of miniJPAS and J-NEP. Values of σ_{NMAD} at the same *odds* agree within their 1-σ uncertainties for all intervals except those centred at *odds*=0.4 and *odds*=0.9 (the excess σ_{NMAD} at *odds*~0.9 in J-NEP also deserves further investigation), despite the differences in depth and recalibration methods. This suggests that the relation between *odds* and σ_{NMAD} is largely insensitive to a change of ~0.5 mag in the depth of the observations and is not strongly affected by the systematic uncertainties resulting from the different recalibration strategies in J-NEP and miniJPAS.

Because of the inevitable small differences in the PSF FWHM and/or depth of the coadded J-PAS images, the S/N of the sources at a given magnitude (and therefore also their photo-*z* accuracy) will vary between pointings. However, since these changes in the quality of the photometry are automatically accounted for by the *odds* parameter, we expect the σ_{NMAD} and η at constant *odds* to remain homogeneous throughout the J-PAS survey.

5.2. Extrapolation to the entire J-NEP

The subsamples with and without spectroscopy in miniJPAS have very similar distributions for the *r*-band magnitude, broadband colours, z_{phot} and *odds*. This allowed HC21 to conclude that the photo-*z* performance in the two subsamples must also be very similar. In the case of J-NEP, we have already shown in Fig. 5

that the distribution of the *g-r* and *r-i* colours in the spectroscopic sample is roughly consistent with that of the entire sample of $P_{star}<0.5$ sources. However, both the *r*-band magnitude and the photo-*z* show highly significant differences in their distributions (see Fig. 14). In particular, only 24% of galaxies in the spectroscopic sample have *r*>22.5 compared to 35% in the full sample. On the other hand, bright galaxies (*r*<21) represent 25.5% of the spectroscopic sample but just 17% of the full sample. This bias towards brighter galaxies is also reflected in the distribution of z_{phot}: 57% of the spectroscopic sample has $z_{phot}<0.5$ compared to just 47% in the full sample.

Since the accuracy of photo-*z* estimates is sensitive to both the magnitude and redshift of the sources (which determine the S/N of the photometry and the spectral features covered by the observed wavelength range, respectively), we can expect that the σ_{NMAD} and η measured in the spectroscopic subsample of J-NEP underestimate their values in the full sample.

To predict the distribution of |Δ*z*| in the full miniJPAS sample, HC21 compensated for the small statistical differences between the samples with and without z_{spec} in miniJPAS by modelling the latter using a random subset of the former with the same distribution of *odds*. Since no significant dependence of σ_{NMAD} or η with other parameters at constant *odds* was found, it was reasonable to assume that two samples with the same *odds* distribution also share a similar distribution of |Δ*z*|. While the spectroscopic subsample of J-NEP is too small to check for variation in the photo-*z* accuracy at constant *odds*, the experience with miniJPAS suggests that such dependence should be small. Therefore, we can predict the distribution of |Δ*z*| (and from it σ_{NMAD} and η) by substituting each of the sources in the full sample with one from the spectroscopic subsample that has similar *odds*[2]. We repeat this source association by *odds* multiple times. The randomness of the process ensures that in each realisation a different subset of the spectroscopic sample is selected and therefore the resulting distribution of Δ*z* changes. This pro-

---

[2] In practice, we define a small tolerance, Δ*odds*=0.005, and pick at random one of the sources within *odds*±Δ*odds*.
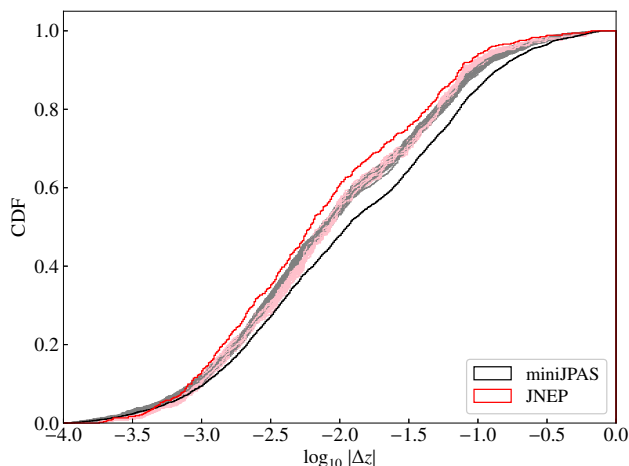
Fig. 15. Cumulative distribution function of photo-z errors in the spectroscopic samples of J-NEP (red) and miniJPAS (black), and predictions for all J-NEP galaxies based on the *odds*-matching with the spectroscopic samples of J-NEP (pink) and miniJPAS (grey).

vides an indication of the statistical uncertainty in the predicted distribution of Δz for the full sample.

The results are shown in Fig. 15. The cumulative distribution functions (CDFs) of $|\Delta z|$ for each of the realisations (pink histograms) are similar in shape, but systematically below the CDF for the spectroscopic sample (red histogram). The predicted σ_{NMAD} for the full sample is $1.16 \pm 0.07 \times 10^{-2}$ compared to 0.88×10^{-2} in the spectroscopic sample. For the outlier rate, the prediction is $\eta = 30.0 \pm 0.7\%$ against $\eta = 25.0\%$ in the spectroscopic sample.

We can also predict the distribution of $|\Delta z|$ in J-NEP with a match by *odds* to the spectroscopic sample in miniJPAS instead of that in J-NEP. The resulting CDFs are shown as grey histograms in Fig. 15. They overlap with the spectroscopic sample of J-NEP in most of the range, but there are small discrepancies at the extremes ($\log_{10} |\Delta z| \lesssim -3$ and $\log_{10} |\Delta z| \gtrsim -1.2$) and also around $\log_{10} |\Delta z| \sim -2.5$. However, the predictions for σ_{NMAD} ($1.13 \pm 0.05 \times 10^{-2}$) and η ($29.0 \pm 0.7\%$) are both consistent within the uncertainties with those from the spectroscopic sample of J-NEP.

Obtaining compatible predictions from the spectroscopic samples in J-NEP and miniJPAS despite the differences in the depth of the images implies that we will be able to evaluate the photo-z performance in individual J-PAS pointings from their *odds* distribution alone, regardless of the availability of spectroscopy.

5.3. Photo-z accuracy in magnitude- and *odds*-limited samples

In the previous section, we estimated that the photo-z of J-NEP sources have typical errors of $\sim 1.1\%$, with a $\sim 30\%$ probability for the error being larger than 3%. While this may suffice for some applications, others require higher accuracy (lower σ_{NMAD}), higher reliability (lower η), or both. This can be achieved, at the cost of sample size, by limiting the selection in magnitude or in *odds*. While a cut in magnitude seems more natural and easier to work with, HC21 showed that cutting in *odds* is significantly more efficient. In Fig. 16, we show σ_{NMAD} and η predicted for a selection of the full J-NEP sample in which
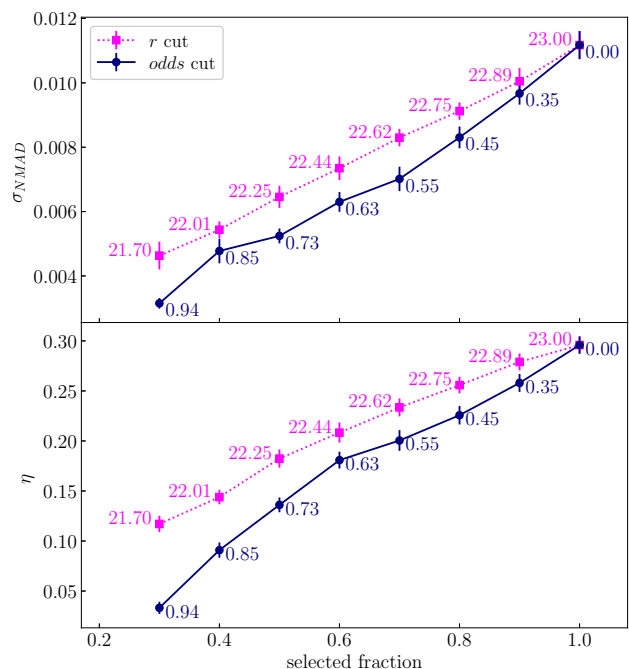
Fig. 16. Dependence of σ_{NMAD} (top panel) and η (bottom panel) on the fraction of the full J-NEP sample selected when a threshold value in the r-band magnitude (squares) or the *odds* parameter (circles) is applied. Each symbol is annotated with the numerical value of the threshold.

a threshold value in *odds* or the r-band magnitude is applied. At any given selection fraction, both σ_{NMAD} and η are consistently lower for an *odds*-based selection. Also, if the goal is to reach some specific value of σ_{NMAD} or η, the fraction of sources selected is consistently larger with an *odds*-based selection.

6. On the nature of photo-z outliers

HC21 proposed three possible reasons for photo-z outliers: degeneracy in the colour space, artefacts in the photometry, and exotic spectra not represented in the template set. In this section we explore in more detail the factors contributing to photo-z outliers using the spectroscopic samples of miniJPAS and J-NEP.

Colour-space degeneracy occurs when the observed photometry of a source can be reproduced with comparably good accuracy (i.e., similar χ^2) by two or more spectral templates at significantly different redshifts. This translates into a likelihood distribution $\mathcal{L}(z) \propto e^{-\chi^2(z)/2}$ with two or more peaks, only one of them matching the actual redshift of the source. Photometric errors and artefacts in the photometry can in some cases induce a better fit (lower χ^2) at the wrong redshift, resulting in a photo-z outlier (see Figure 17).

The redshift prior modulates $\mathcal{L}(z)$ by penalising values of z that imply a very high or very low luminosity at a given magnitude. For bright sources, the resulting $P(z)$ sees a decrease in the strength of peaks at high z compared to $\mathcal{L}(z)$. For fainter ones, peaks at low z are suppressed. While this decreases the frequency of spurious solutions in normal galaxies, it also makes harder to select the correct peak for low z sources with unusually low luminosity, like dwarf galaxies.

The impact of the prior in the outlier rate is evident in Figure 18. For each magnitude bin, the minimum η is obtained at a redshift close to the peak probability of the prior for that magnitude (see Fig. 7 in HC21). The effect is most dramatic in the
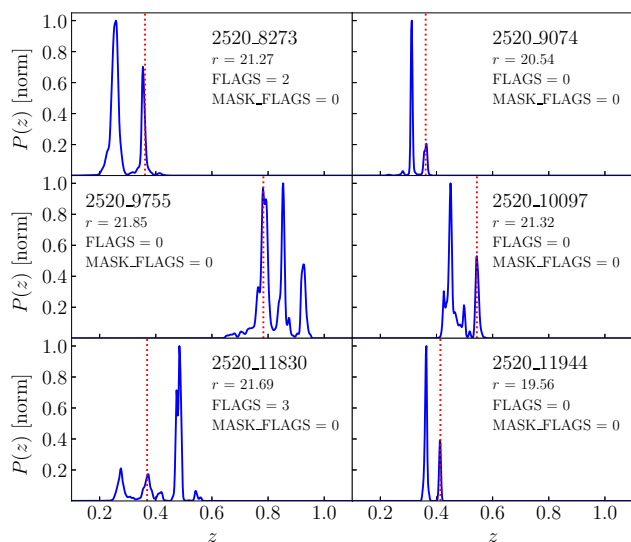
Fig. 17. Examples of zPDFs for J-NEP sources in which the spectroscopic redshift (dotted line) matches a secondary peak of the zPDF.
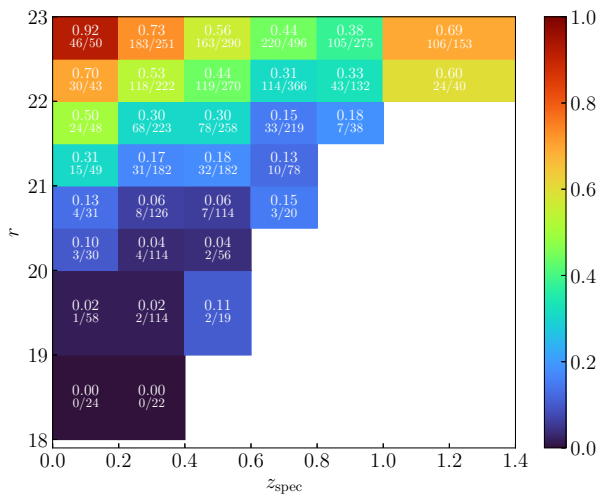

Fig. 18. Colour-coded map of the outlier rate as a function of r-band magnitude and redshift for the combined spectroscopic samples of mini-JPAS and J-NEP. The colour of each rectangular region represents the frequency of outliers ($|\Delta z|>0.03$) among sources inside that region.

faintest magnitude bin (r=22.5–23), where the outlier rate increases from η=0.38 at z=0.8–1 to η=0.92 at z=0–0.2. The dependence of η with z at constant magnitude is an expected consequence of having a redshift prior and does not imply that the prior or the zPDFs are biased. The top panel in Figure 19 shows that for the 21<r<22 range, the distribution of z_{phot} agrees with that for z_{spec} as well as with the combined zPDF of all the galaxies in that magnitude range (in other words, taking the mode of the zPDF does not bias the results against low redshift galaxies). However, in the magnitude range 22<r<23 both the combined zPDF and the distribution of z_{phot} predict far fewer galaxies at z<0.36 than observed. This suggests the prior might underestimate their number density, albeit a selection effect in the spectroscopic sample might also explain the discrepancy (Hα exits the spectroscopic range at z~0.38, making more difficult to obtain a high confidence z_{spec} at faint magnitudes).
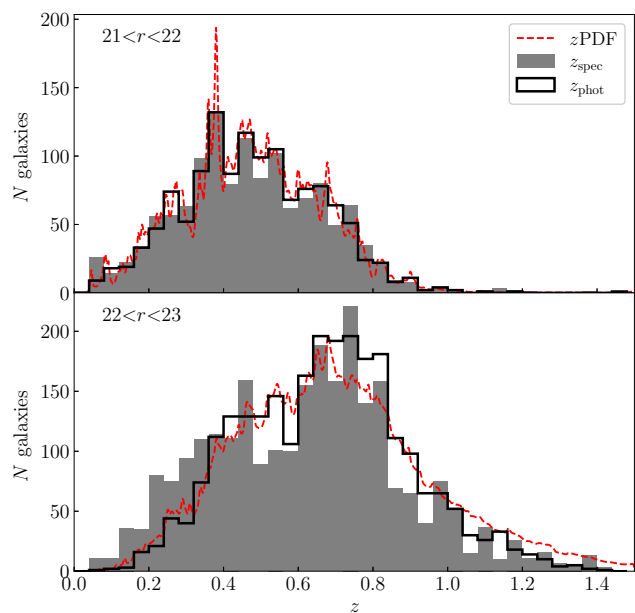
Fig. 19. Redshift distribution for galaxies in the combined spectroscopic samples of miniJPAS and J-NEP for the magnitude bins 21<r<22 (top) and 22<r<23 (bottom). The grey bars and solid black lines indicate the distribution of z_{spec} and z_{phot}, respectively. The dashed red line represent the combined zPDFs for the galaxies in the magnitude bin.
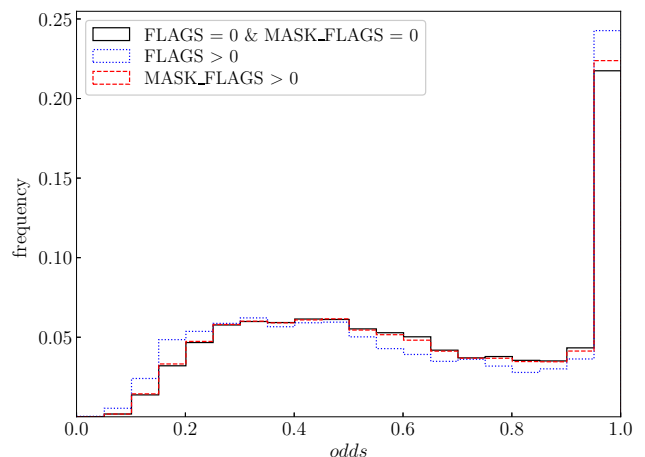
Fig. 20. Distribution of *odds* for galaxies in the combined sample of miniJPAS and J-NEP sources with r<23, separating flagged and non-flagged sources using the FLAGS and MASK_FLAGS parameters (see text for details). Each source is weighted with its P_{gal}.

Figure 18 also shows a sudden increase in η at z>1 compared to the z=0.8–1 interval. The redshift prior is unlikely to be responsible for this since it decreases smoothly towards higher z. A more likely interpretation is the shift outside of the J-PAS wavelength range of another useful spectral feature, the 4000 Å break, at z~1.2. While the [O II] 3727 Å line allows for reliable z_{spec} up to z~1.4, in most cases it is not strong enough for detection in the reddest narrow band filters of J-PAS.

The second proposed cause for outliers, artefacts in the photometry, includes any circumstances that introduce errors in the observed photometry not accounted for by the nominal photometric uncertainty. These may include: systematics in the photo-
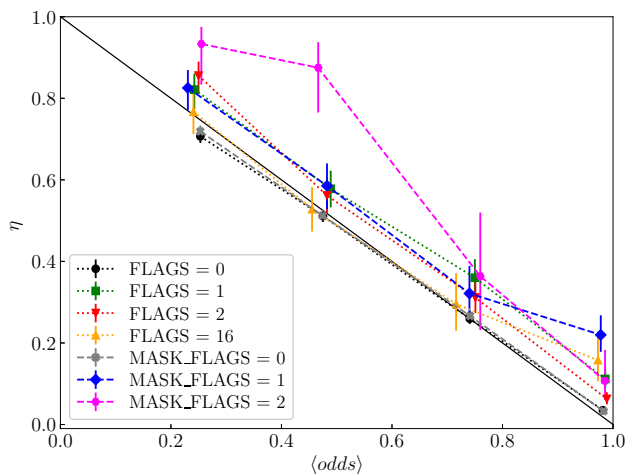
Fig. 21. Relation between the outlier rate and the average *odds* for sources grouped by their flags values. Symbols indicate the fraction of outliers found in the combined spectroscopic sample of miniJPAS and J-NEP for sources in the *odds* intervals 0–0.35, 0.35–0.6, 0.6–0.9, and 0.9–1. Error bars represent 68% confidence intervals computed with the Wilson formula for binomial distributions. The solid line represents the relation $\eta = 1 - \langle odds \rangle$.

metric calibration, inaccurate background subtraction, contamination from nearby sources, saturation, residuals from cosmic rays, defects in the CCD, etc.

Some of these issues are identified by the data reduction pipeline or SExtractor and stored in the MASK_FLAGS or FLAGS parameters, respectively (see Bonoli et al. 2021, for details). MASK_FLAGS = 1 indicates the source is close to the borders of the image, while sources affected by saturated stars have MASK_FLAGS = 2. The most relevant SExtractor flags are FLAGS = 1 (photometry likely biased by neighbouring sources or by more than 10% of bad pixels in any aperture), FLAGS = 2 (the object has been deblended), and FLAGS = 16 (at least one photometric aperture is incomplete or corrupted). The flags are additive. Sources with no detected issues have MASK_FLAGS = 0 and FLAGS = 0.

The impact of flagged issues in the photo-*z* is small for most of the sources. Figure 20 shows that the distribution of the *odds* parameter for sources with MASK_FLAGS > 0 is consistent with that for sources with no flags. Sources with FLAGS > 0, on the other hand, have a higher probability of obtaining either very low (<0.25) or very high *odds* (>0.95).

Figure 21 shows that flagged sources have a ~10% chance for catastrophic redshift errors additional to the outlier probability predicted from the *odds*. There is no clear dependence with the type of flags or the *odds* value, except for sources near saturated stars (MASK_FLAGS = 2), which at low *odds* are almost invariably outliers. The ~10% increase in η implies that the photo-*z* of flagged sources with very high *odds* are not as reliable as the *odds* suggests. Therefore, flagged sources should be excluded from the sample selection for those applications that demand a very low outlier rate ($\eta \lesssim 0.1$). The top left panel in Fig. 22 shows an example of a galaxy contaminated by a nearby star that obtains a very high confidence photo-*z* at a wrong redshift.

The third cause for outliers is exotic spectra not represented in the template set. By definition, those sources will have a poor fit at all redshifts. However, this does not prevent them from obtaining high *odds*, since the shape of the *z*PDF depends on the

relative (not absolute) values of $\mathcal{L}(z)$ at each *z*. In particular, both stars and quasars often obtain very high *odds* (including *odds* = 1) at wrong redshifts. However, we do not consider them as legitimate outliers since, by construction, our photo-*z* measurements are conditional to the sources actually being galaxies.

In some cases, SExtractor can detect close pairs of stars as a single extended source, which can get a very low P_{star} value. A related case is that of a galaxy with a star in the foreground, or two galaxies at different redshifts that overlap in projection and get classified as a single extended source. We consider these as detection errors or contamination issues, not exotic spectra. An interesting example is shown in the middle panel of Fig. 22. SExtractor detects as an elongated source what is actually two or three galaxies in close proximity, as shown in superb detail in the JWST/NIRCAM images (Fig. 23). The centroid of the J-NEP detection is very close to the bluer galaxy to the West, which might dominate the flux in the PSFCOR aperture. The Binospec spectrum, centred on the same galaxy, shows a post-starburst spectrum with strong Mg II $\lambda\lambda2796, 2803$ Å and Balmer absorption lines as well as [O II] and [O III] emission. Other post-starburst galaxies that obtain their best fit with the same spectral template have accurate photo-*z*, suggesting that contamination from the red galaxy to the East is the cause for the outlier. We note that while the peak at *z*=0.832 completely dominates the *z*PDF, there is a second peak with *P(z)*=0.025 that is consistent with the spectroscopic redshift.

A legitimate example of a galaxy with an exotic spectrum resulting in a wrong photo-*z* at high *odds* is shown in the top right panel of Fig. 22. The source is barely resolved in the J-NEP images (P_{star}=0.77) and is classified as a star by SDSS. However, the Binospec spectrum shows very strong [O III] $\lambda\lambda4959, 5007$ Å lines (which cause the excess flux observed in the J0760 and J0770 bands). Hα is redshifted out of the J-PAS and spectroscopic wavelength ranges, but the high [O III] equivalent width and the colours in the WISE bands suggest it is an AGN (albeit it is not detected by NuSTAR). Since there are no templates with such strong [O III] emission in our template set, LePhare misidentifies the excess in J0760 and J0770 as Hα at *z*~0.15.

7. Summary and conclusions

This paper presents the photometry and photometric redshifts of J-NEP, a survey of ~0.3 deg^2 centred on the JWST Time Domain Field in the North Ecliptic Pole performed with the Pathfinder camera on the JST/T250 telescope. Similarly to mini-JPAS (Bonoli et al. 2021), J-NEP observes in the 56 narrow-bands of J-PAS, plus *u*, *g*, *r*, and *i*, but reaches ~0.5–1.0 magnitudes deeper, depending on the filter, with a typical PSF FWHM of ~1.2″.

J-NEP provides single-band source catalogues in the 60 filters as well as forced (dual mode) photometry in several apertures for the 24,618 sources detected in the *r*-band image. All sources are classified as stars or galaxies using the neural network classifier of SExtractor and the star probabilities of the Stellar-Galaxy Locus Classification of López-Sanjuan et al. (2019b).

We present a new method for correcting systematic offsets in the colours from PSF-corrected (PSFCOR) photometry, dubbed "galaxy locus recalibration". The method relies on the recalibration method proposed in HC21 to determine the median colours of galaxies (the "galaxy locus") in a reference sample. Then, it computes the magnitude offsets that, when applied to the observed photometry, make the median colours match the galaxy
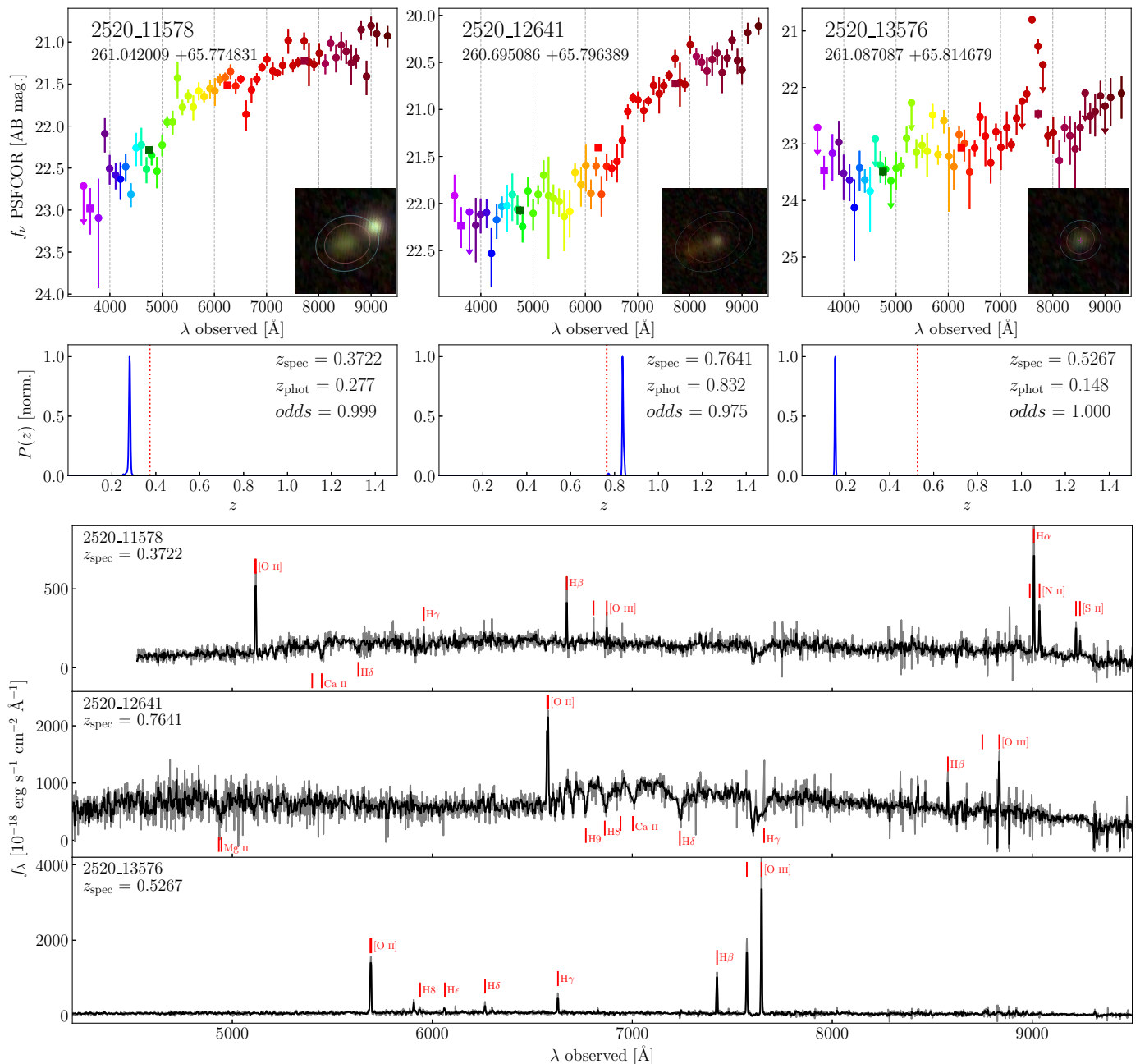
Fig. 22. Examples of J-NEP galaxies with high confidence photo-z at an incorrect redshift. The top panels show their 60-band spectral energy distributions from J-PAS. Coloured circles (squares) indicate the PSFCOR magnitude in the narrow- (broad-) band filters. Error bars and arrows represent 1-σ uncertainties and 3-σ upper limits, respectively. Cutout images are a composite of the g (blue), r (green), and i (red) bands. The red ellipses represent the 2 Kron radii apertures used to extract AUTO photometry. The PSFCOR apertures are half their size (1 Kron radius). The middle panels show the normalised zPDF (solid line). The spectroscopic redshift is indicated with a vertical dotted line. The bottom panel shows the spectra from MMT/Binospec (Willmer et al. in preparation). The original spectrum (grey line) has been smoothed with a 5-element median filter to improve visualisation (black line). Red vertical lines mark some of the emission and absorption lines.

locus. While this new recalibration strategy is less accurate, it is applicable to any J-PAS pointing regardless of the availability of spectroscopy.

We obtain photo-z for all 6,662 J-NEP sources brighter than r=23. The photo-z are computed by a customised version of LePHARE with the same configuration options used for miniJPAS, including the same 50 galaxy templates generated from a selection of miniJPAS galaxies and redshift priors derived from VVDS. The distribution of photo-z for J-NEP galaxies is consistent with that found in miniJPAS, except for faint (r>22) sources, where

J-NEP shows an excess of sources at $z_{\rm phot}$<0.2 and a deficit at $z_{\rm phot}$>1 relative to miniJPAS. Both are likely due to higher S/N in the photometry allowing for more robust photo-z estimates.

We use a sample of 787 galaxies with reliable spectroscopic redshifts taken from the redshift catalogue in Willmer et al. (in preparation) to validate the accuracy of J-NEP photo-z. No spectroscopic information on the J-NEP sources was available to the photo-z team before completion of the final photo-z catalogue. This allows us to ensure that the photo-z accuracy measured in the spectroscopic subsample is not affected by overfitting. 76%
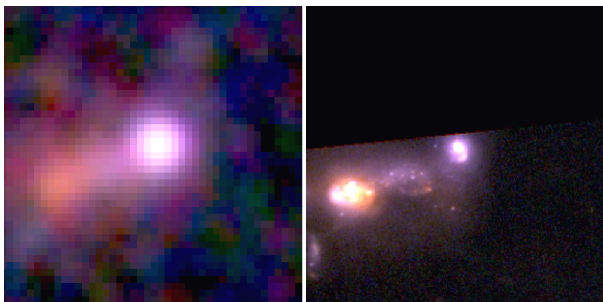
Fig. 23. 10×10″ cutouts centred around the coordinates of the source 2520_12641. The left panel is a composite of the J-NEP bands *g* (blue), *r* (green), and *i* (red), smoothed with a top-hat filter. The right panel is a composite of the JWST/NIRCAM bands F090W (blue), F150W (green), and F200W (red) from JWST proposal 2738 (Windhorst et al. 2023). North is up, East is left.

of the spectroscopic sources have photo-*z* error $\Delta z < 0.03$, consistent with the expectation from the average *odds* of the sample $\langle odds \rangle = 0.771$.

The typical Δz (σ_{NMAD}) and the frequency of outliers (η) are slightly higher compared to miniJPAS for $r < 21.5$, probably due to larger systematic errors, but they are up to ∼30–50% lower at fainter magnitudes. This suggests that the higher S/N resulting from deeper observations, particularly in the redder bands, has a strong impact in the photo-*z* accuracy of faint sources.

Despite the differences in depth and systematic uncertainties, the dependence of σ_{NMAD} with *odds* in J-NEP is consistent within the uncertainties with that measured in miniJPAS. Furthermore, we predict the distribution of Δz for the entire J-NEP sample using as reference the spectroscopic samples of J-NEP and miniJPAS and arrive at very similar results. Combined with a lack of dependence of σ_{NMAD} on the magnitude or the spectral type of the sources at constant *odds*, this suggests that we will be able to predict the σ_{NMAD} of any set of J-PAS sources from their *odds* distribution alone, with no need for additional spectroscopy to calibrate the relation between *odds* and Δz.

We explore the factors contributing to photo-*z* outliers in J-NEP and miniJPAS. For faint sources, the main reason is colour-space degeneracy due to large uncertainties in the observed colours. This is exacerbated in low *z* dwarf galaxies by an unfavourable redshift prior and at high *z* by the shift of key spectral features outside of the J-PAS wavelength range. At brighter magnitudes, artefacts in the photometry (including those signalled by the photometry flags) and exotic spectra not represented in the template set contribute most of the outliers with high *odds*.

The photometry and photo-*z* presented in this paper are being used in multiple science projects by the J-PAS collaboration, including the search and characterisation of Lyman alpha emitters in miniJPAS and J-NEP (Torralba et al. in preparation), a census of extreme emission line galaxies at *z*<0.8 (Arroyo Polonio et al. in preparation), the characterisation of the stellar population and emission line properties of J-NEP galaxies (González Delgado et al. in preparation) and the 3-D distribution and clustering properties of J-NEP galaxies (Maturi et al. in preparation).

All miniJPAS data, including images, catalogues, and value-added data products, are publicly available through the CEFCA catalogues portal[3]. Access to J-NEP data can be granted for specific use upon request to the science directors of J-PAS prior to the official public release currently scheduled for the third quar-

ter of 2023. The JWST data are publicly available from the Space Telescope Science Institute MAST Archive[4].

References

Arnouts, S., & Ilbert, O. 2011, LePHARE: Photometric Analysis for Redshift Estimate, ascl:1108.009
Baqui, P. O., Marra, V., Casarini, L. et al. 2021, A&A, 645, 87B
Benítez, N., Moles, M., Aguerri, J. A. L., et al. 2009, ApJ, 692, L5
Benítez, N., Dupke, R., Moles, M., et al. 2014, arXiv e-prints, arXiv:1403.5237
Bertin, E. & Arnouts, S. 1996, A&AS, 117, 393
Bertin, E., Mellier, Y., Radovich, M., et al. 2002, Astronomical Data Analysis Software and Systems XI, 281, 228
Bertin, E. 2006, Astronomical Data Analysis Software and Systems XV, 351, 112
Bonoli, S., Marín-Franch, A., Varela, J., et al. 2021, A&A, 653, A31
Boquien, M., Burgarella, D., Roehlly, Y., et al. 2019, A&A, 622, A103
Cenarro, A. J., Moles, M., Marín-Franch, A., et al. 2014, SPIE Conf. Ser., 9149, 91491I
Chaves-Montero, J., Bonoli, S., Trakhtenbrot, B., et al. 2022, A&A, 660, A95
Coe, D., Benítez, N., Sánchez, S. F., et al. 2006, AJ, 132, 926
Fabricant, D., Fata, R., Epps, H., et al. 2019, PASP, 131, 075004
González Delgado, R. M., Díaz-García, L. A., de Amorim, A., et al. 2021, A&A, 649, A79
González Delgado, R. M., Rodríguez-Martín, J. E., Díaz-García, L. A., et al. 2022, A&A, 666, A84
Green, G. M., Schlafly, E. F., Finkbeiner, D., et al. 2018, MNRAS, 478, 651
Hernán-Caballero, A., et al. 2021, A&A, 654, 101
Iglesias-Páramo, J., Arroyo, A., Kehrig, C., et al. 2022, A&A,

---

Jansen, R. A. & Windhorst, R. A. 2018, PASP, 130, 124001
Kansky, J., Chilingarian, I., Fabricant, D., et al. 2019, PASP, 131, 075005
Laur, J., Tempel, E., Tamm, A., et al. 2022, A&A, 668, A8
Le Fèvre, O., Vettolani, G., Garilli, B., et al. 2005, A&A, 439, 845
López-Sanjuan, C., Varela, J., Cristóbal-Hornillos, D., et al. 2019a, A&A, 631, A119
López-Sanjuan, C., Vázquez Ramió, H., Varela, J., et al. 2019b, A&A, 622, A177
López-Sanjuan, C., Yuan, H., Vázquez Ramió, H., et al. 2021, A&A, 654, A61
Martínez-Solaeche, G., González Delgado, R. M., García-Benito, R., et al. 2021, A&A, 647, A158
Martínez-Solaeche, G., González Delgado, R. M., García-Benito, R., et al. 2022a, A&A, 661, A99
Molino, A., Costa-Duarte, M. V., Mendes de Oliveira, C., et al. 2019, A&A, 622, A178
Newman, J. A., Cooper, M. C., Davis, M., et al. 2013, ApJS, 208, 5
Polsterer, K. L., D'Isanto, A., & Gieseke, F. 2016, arXiv:1608.08016
Queiroz, C., Abramo, L. R., Rodrigues, N. V. N., et al., 2022, MNRAS in press (arXiv:2202.00103)
Rodríguez-Martín, J. E., González Delgado, R. M., Martínez-Solaeche, G., et al. 2022, A&A, 666, A160
Schlafly, E. F., Meisner, A. M., Stutz, A. M., et al. 2016, ApJ, 821, 78
Whitten, D. D., Placco, V. M., Beers, T. C., et al. 2019, A&A, 622, A182
Windhorst, R. A., Cohen, S. H., Jansen, R. A., et al. 2023, AJ, 165, 13
Xiao, K., Yuan, H., Varela, J., et al. 2021, ApJS, 257, 31

[1] Centro de Estudios de Física del Cosmos de Aragón (CEFCA), Plaza San Juan, 1, E-44001 Teruel, Spain

[2] Steward Observatory, University of Arizona, 933 North Cherry Avenue, Tucson, AZ 85721, USA

[3] Centro de Estudios de Física del Cosmos de Aragón (CEFCA), Unidad Asociada al CSIC, Plaza San Juan, 1, E-44001 Teruel, Spain

[4] Donostia International Physics Centre, Paseo Manuel de Lardizabal 4, E-20018 Donostia-San Sebastian, Spain

[5] Ikerbasque, Basque Foundation for Science, E-48013 Bilbao, Spain

[6] Observatório Nacional, Ministério da Ciência, Tecnologia, Inovação e Comunicações, Rua General José Cristino, 77, São Cristóvão, 20921-400, Rio de Janeiro, Brazil

[7] Department of Astronomy, University of Michigan, 311 West Hall, 1085 South University Ave., Ann Arbor, USA

[8] Department of Physics and Astronomy, University of Alabama, Box 870324, Tuscaloosa, AL, USA

[9] Department of Physics, University of Hong Kong, 852-2219 4924, HK

[10] Tartu Observatory, University of Tartu, Observatooriumi 1, 61602 Tõravere, Estonia

[11] Departamento de Astrofísica, Universidad de La Laguna, E-38206, La Laguna, Tenerife, Spain

[12] Instituto de Astrofísica de Canarias, E-38200 La Laguna, Tenerife, Spain

[13] Instituto de Física de Cantabria (Consejo Superior de Investigaciones Científicas - Universidad de Cantabria). Avda. de los Castros, E-39005, Santander, Spain

[14] Unidad Asociada "Grupo de astrofísica extragaláctica y cosmología" (IFCA - Universitat de València). Parc Científic UV, E-46980, Paterna, Spain

[15] Instituto de Astrofísica de Andalucía (CSIC), P.O. Box 3004, E-18080 Granada, Spain

[16] Instituto de Física, Universidade de São Paulo, Rua do Matão 1371, CEP 05508-090, São Paulo, Brazil

[17] Departamento de Astronomia, Instituto de Física, Universidade Federal do Rio Grande do Sul (UFRGS), Av. Bento Gonçalves 9500, Porto Alegre, R.S, Brazil

[18] Instituto de Física, Universidade Federal da Bahia, 40210-340, Salvador, BA, Brazil

[19] Departamento de Astronomia, Instituto de Astronomia, Geofísica e Ciências Atmosféricas da USP, Cidade Universitária, 05508-900, São Paulo, SP, Brazil

[20] Instruments4, 4121 Pembury Place, La Cañada-Flintridge, CA, 91011, USA
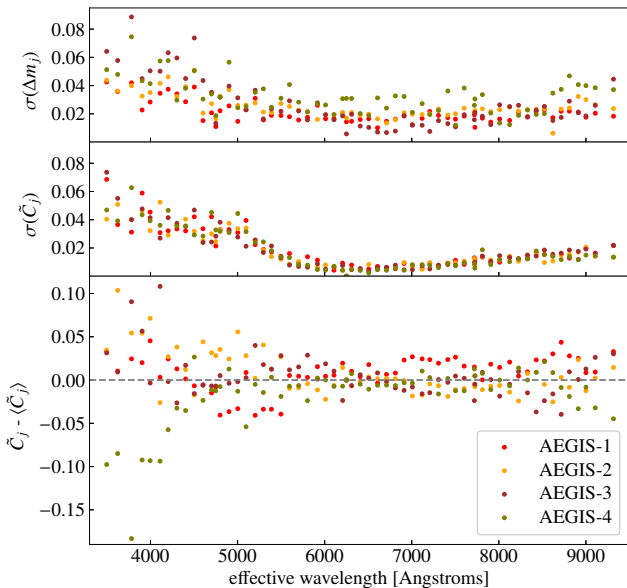
Fig. A.1. Top panel: 1-σ uncertainty in the recalibration offsets for individual miniJPAS pointings (from HC21). Middle panel: 1-σ uncertainty in the median observed colours, C_j, of the galaxies with $r<21$ in each miniJPAS pointing. Bottom panel: dispersion between the galaxy loci obtained on individual miniJPAS pointings.

Appendix A: Accuracy of recalibration with the galaxy locus

In the ISMFR method based on SPS model fits that was presented in HC21, the magnitude offset for band j in a given pointing, Δm_j, is computed as the median difference between the observed magnitudes and those predicted from the SPS models for a sample of spectroscopic galaxies. The uncertainty in Δm_j, $\sigma(\Delta m_j)$, depends on the photometric errors of the individual galaxies and the number of spectroscopic galaxies available (note that only $r<22$ galaxies are used due to very large photometric errors for the narrow bands in the fainter ones). The statistical uncertainty in the recalibration with this method is $\sigma(\Delta m_j)$ ∼ 0.02 mag except for the bluest bands, where the photometric errors of individual galaxies are larger (see top panel in Fig. A.1).

The galaxy locus recalibration (GLR) inherits this uncertainty as a systematic offset in the colour of all the galaxies in a given pointing. In addition, GLR is affected by the statistical uncertainty, $\sigma(\tilde{C}_j)$, in the determination of the median colour of the $r<21$ galaxy sample. We estimate $\sigma(\tilde{C}_j)$ for each miniJPAS pointing with bootstrap resampling (middle panel). The total uncertainty of the galaxy locus defined on a single pointing is thus

$$\sigma_{tot}(\tilde{C}_j) = \sqrt{\sigma^2(\Delta m_j) + \sigma^2(\tilde{C}_j)} \tag{A.1}$$

Using the galaxy locus defined from one pointing to recalibrate another one means that cosmic variance may also have an impact on the results. The bottom panel in Fig. A.1 shows the dispersion in $\tilde{C}_j$ values among the individual miniJPAS pointings. The median absolute difference in $\tilde{C}_j$ between any two miniJPAS pointings is 0.031 mag (standard deviation: 0.046 mag), again dominated by the bluer bands. To test whether cosmic variance or other sources of error not included in $\sigma_{tot}(\tilde{C}_j)$
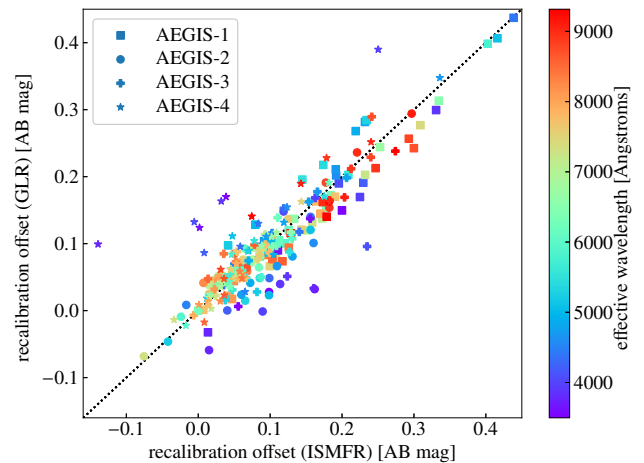
Fig. A.2. Comparison of the magnitude corrections determined for each band for individual miniJPAS pointings using the original recalibration method presented in HC21 (ISMFR) and the recalibration with galaxy locus from this work (GLR).

contribute significantly to this dispersion, we compute for each pair (a, b) of miniJPAS pointings the reduced χ^2 statistic

$$\chi_r^2(a, b) = \frac{1}{n_j - 1} \sum_{j=1}^{n_j} \frac{(\tilde{C}_j^a - \tilde{C}_j^b)^2}{\sigma_{tot}^2(\tilde{C}_j^a) + \sigma_{tot}^2(\tilde{C}_j^b)} \tag{A.2}$$

The values of χ_r^2 range from 0.54 to 1.04, suggesting that differences in $\tilde{C}_j$ between pointings are entirely accounted for by the uncertainties of the ISMFR method and the statistical uncertainty in the median colours.

As a final test, we compute recalibration offsets with the GLR method for all four miniJPAS pointings. For each of them we use the galaxy locus obtained from the other three pointings. In Fig. A.2 we compare the magnitude offsets obtained with the ISMFR and GLR methods. The 1-σ dispersion in the difference between the two methods is 0.039 mag, dominated by the bluest bands. If we consider only bands with $\lambda_{eff}>4500$ Å the dispersion decreases to 0.024 mag. This is comparable to the uncertainty in the ISMFR method and implies that the total systematic error in galaxy colours with the GLR method is at most ∼0.04–0.05 mag.